Chinese Chemical Letters 32 (2021) 3277–3287

Contents lists available at ScienceDirect

Chinese Chemical Letters

journal homepage: www.elsevier.com/locate/cclet

Review

The applications of semiconductor materials in air batteries

Yingjian Yu [a], Sujuan Hu [b,*]

[a] School of Physical Science and Technology, Kunming University, Kunming 650214, China
[b] School of Chemistry and Chemical Engineering, Kunming University, Kunming 650214, China

ARTICLE INFO

Article history:
Received 20 January 2021
Revised 24 February 2021
Accepted 25 April 2021
Available online 2 May 2021

Keywords:
Si-air battery
Ge-air battery
Li-O_2 battery
Zn-air battery
Semiconductors
Catalysts
Photo-assistance

ABSTRACT

Air batteries are promising energy storage technologies that have gained continuous attraction due to their high energy densities. At present, investigations on anodes of air batteries are usually focused on various metals such as Li, Zn, Al. In contrast, the semiconductor anodes like Si and Ge are less investigated. Si-air battery possesses a high theoretical energy density and Ge-air battery has a high actual power density and ideal safety. Besides anodes, air cathodes where oxygen reduction reaction (ORR) and oxygen evolution reaction (OER) are also the key components in air batteries. To further promote the discharging performance and facilitate energy conversion/storage, semiconductor materials have been introduced in electrochemical cells like Li-O_2 and Zn-air batteries. This review briefly summarizes semiconductor materials utilized in various air batteries, including the progress of Si-air and Ge-air batteries and recent advances in semiconductor cathodes catalysts. Finally, the remaining challenges and further perspective are discussed.

1. Introduction

During the past few decades, greenhouse-gas concentration has dramatically increased with severe consequences like the global warming [1]. Fortunately, opportunities still exist if the consumption of fossil fuels is decreased. Although fossil fuels still play a significant role in the global energy demand, the world is gradually heading for green energies for the betterment of the environment [2]. Nowadays, from portable electronic devices to automotive vehicles, lithium ion batteries (LIBs) have been widely applied given their high energy efficiency and long working life [3–5]. It is predicted that the market size of LIBs will reach $99.98 billion in 2025 [6]. Such huge demand will inevitably result in enormous consumption of raw materials, especially lithium and cobalt [7,8]. The average price of Co was $75,991.27/t in 2018 and for battery-grade Li_2CO_3 the export price reached $12,514/t in 2019 [6]. Moreover, because of fundamental chemical limitations, the available LIBs technology cannot entirely meet the improving requirements of electric vehicles in the future [9]. Therefore, researches on potential next-generation batteries with higher energy density and lower cost are urgent demands [10–16].

In recent years, air batteries as kinds of promising energy storage technologies have gained continuous attraction owing to their high energy densities [17–21]. Since they can utilize O_2 from the atmosphere, the traditional cathode chamber can be discarded, resulting in theoretical energy densities 3–30 times higher than those of LIBs. Generally, an air battery is composed of an anode with suitable electrolyte and a porous air cathode containing oxygen electrocatalysts. At present, explorations on air batteries are usually focused on the cells with various metal anodes such as Li, Na, Zn, Al, Mg and Fe, which have been systematically and profoundly discussed in recent reviews [22–41]. Reversible metal-air batteries are supposed to meet some requirements such as a high recharging efficiency, a high anode utilization and a long cycling life. Most challenges of developing metal-air batteries are related to metal anodes. In some kinds of metal-air batteries (*e.g.*, Li-O_2 and Zn-air batteries), the dendrite problem has attracted most attention. The metal dendrites would result in degradations in Coulombic efficiency, specific capacity, stability, and so forth. Meanwhile, the influence of H_2O, CO_2 and N_2 on metal electrode stability cannot be neglected when cells are operated in ambient air. Corrosion is also ubiquitous in aqueous metal-air batteries that brings about self-discharge. Additionally, the anode passivation reduces the depth of discharge and practical energy density.

In contrast, the semiconductor anodes like Si and Ge are less investigated. Silicon is the second most abundant element on earth and the Si-air battery possesses a high theoretical energy density (8461 Wh/kg) [41,42]. Meanwhile, Ge-air battery has a high actual power density (757.7 μW/cm^2) and ideal safety [43].

* Corresponding author.
E-mail address: sujuanhu@yahoo.com (S. Hu).

https://doi.org/10.1016/j.cclet.2021.04.049
1001-8417/

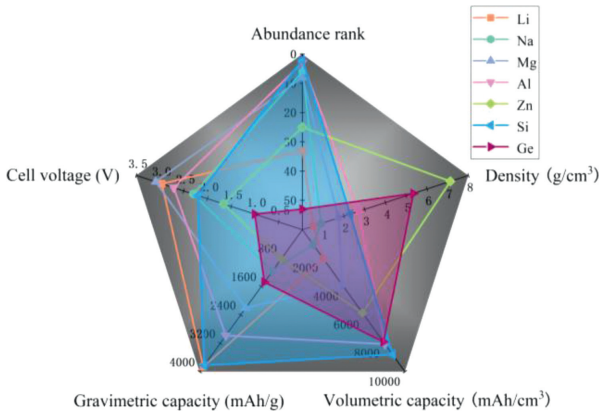

Fig. 1. Multi-measure radar chart of the properties of various air batteries.

A comparison of the properties of various air batteries is shown in Fig. 1. Si-air and Ge-air batteries have larger volumetric capacity than most of the metal-air batteries. Meanwhile, Li-air and Si-air batteries have outstanding gravimetric capacities among all the air batteries. Mg-air and Li-air batteries have advantages in cell voltage. What makes Si and Ge special is that they are compatible with the fast-growing micro/nano-electro-mechanical system (M/NEMS) technologies [44–47]. Consequently, the Si-air and Ge-air battery would be feasibly integrated with other micro/nano-electronic devices.

Besides anodes, air cathodes are also the key components in air batteries [48–51]. The ORR or OER catalysts (*e.g.*, noble metals, metal oxides and carbon materials) in the cathode determine the durability and efficiency of the air batteries, which have been summarized in previous reviews [52–58]. More recently, to further promote the discharging performance and facilitate energy conversion/storage, increasing interests have been focused on applying photocatalysts based on semiconductor materials in electrochemical cells like Li-O_2 and Zn-air batteries [59–61]. The photoelectric effects endow the air/oxygen batteries with photo-responsive functions for potential applications in electronic/optoelectronic devices.

Some excellent reviews relative to Si-air, photo-assisted Li-oxygen and Zn-air batteries have been published of late [41,59,60]; however, as far as we know, few works specially concentrated on the semiconductor materials in air batteries including both anodes and cathodes have been conducted yet. Thus, in this report, we render a brief description of semiconductor materials utilized in various air batteries, including the progress of Si-air and Ge-air batteries and recent advances in semiconductor cathode catalysts. Finally, the remaining challenges and further perspective are discussed.

2. Semiconductor anodes in air batteries

2.1. Si-air batteries

2.1.1. Overview

Silicon was first adopted as the anode of an air battery by Ein-Eli's group in 2009 [62]. In that attempt, planar Si (100) wafers doped by As and B were employed with the electrolyte of room temperature ionic liquid (RTIL) EMI·$(HF)_{2.3}$·F, yielding an average working potential of 1–1.2 V and a discharge time of more than 300 h. Encouraged by that, various investigations on Si batteries have been reported since then as summarized in Table 1. As a semiconductor, it is essential to introduce dopants to enhance the conductivities of silicon anodes. Hence researches on the dopant types and concentrations have been conducted by galvanostatic discharge and potentiodynamic polarization experiments. Usually,

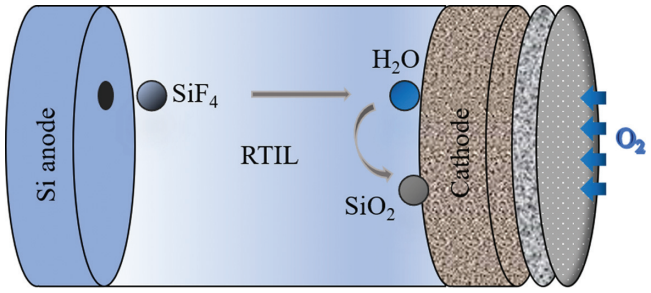

Fig. 2. The representation of the discharging processes of a typical Si-air battery with the EMIm$(HF)_{2.3}$F electrolyte.

the application of the promising Si-O_2 redox-couple relies on the reactions between Si anodes and non-aqueous electrolytes RTIL or aqueous alkaline electrolytes KOH [41]. RTIL exhibits some unusual properties like low viscosity and chemical stability in air and KOH solutions own superior ionic conductivities and less cost that have been extensively used in divalent and multivalent metal-air batteries such as Zn-air, Fe-air and Al-air batteries [17,39]. The same fundamental mechanisms that the silicon is oxidized at the anode and oxygen is reduced at the cathode are presented in both non-aqueous and aqueous electrolytes. However, their concrete reactions are absolutely different. Taking it into consideration, the developments of Si-air batteries will be reviewed individually classified by those two systems in next sections.

2.1.2. Non-aqueous batteries

The non-aqueous batteries are composed of three key parts: the anode of Si wafer, the electrolyte of RTIL and the cathode of carbon-based air electrode, as shown in Fig. 2. During the discharge process, Si is oxidized to Si^{4+} at anode while H_2O and di-hydrogenated fluoride anions are produced *via* the oxygen reduction in the presence of tri-hydrogenated fluoride at the cathode. Furthermore, SiF_4 initially formed at the silicon-electrolyte reacts with water to form silicon dioxide as the end discharge product at the electrolyte-air electrode interface [41]. The electrochemical reactions are proposed below Eqs. 1–4:

$$\text{Anode: Si} + 12(HF)_2F^- \rightleftharpoons SiF_4 + 8(HF)_3F^- + 4e \quad (1)$$

$$\text{Cathode: } O_2 + 12(HF)_3F^- + 4e^- \rightleftharpoons 2H_2O + 16(HF)_2F \quad (2)$$

$$SiO_2 \text{ formation : } SiF_4 + 2H_2O + 4(HF)_2F^- \rightarrow SiO_2 + 4(HF)_3F^- \quad (3)$$

$$\text{Overall cell reaction: Si} + O_2 \rightleftharpoons SiO_2 \quad (4)$$

The feasibility of the RTIL EMI·$(HF)_{2.3}$F as the electrolyte in a Si-air cell was evaluated by conducting potentiodynamic polarization measurements of the RTIL-Si and RTIL-oxygen couples individually [62]. With the theoretical cell voltage of around 2.2 V calculated by applying the Gibbs free energy formula ($\Delta G = -nEF$) to the overall cell reaction, the potential difference of 1.25–1.5 V was found between the anode and the cathode. During those measurements processes, compared with both n^{++} and p^{++} heavily doped Si (100) wafers only n medium-doped Si (100) wafers were passivated. Meanwhile, there was a dilemma that n-type silicon-based cell produce higher voltages at current densities < 1 mA/cm^2 while the p-type Si anode was favored at higher current loads. Subsequently the discharge properties of the n^{++}-Si as anode in a full

Table 1
Summary of performances of semiconductor-air batteries.

Type of battery	Type of anode	Electrolyte	Current density (μA/cm^2)	Open circuit potential (V)	Working potential (V)	Discharge time (h)	Ref.
Si-air battery	n^{++} Si (100)	EMI·$(HF)_{2.3}$F	100	1.55	~ 1.1	350	[62]
Si-air battery	n^{++} As-doped Si (100)	EMI·$(HF)_{2.3}$F	10	1.4	~ 1.1	600	[63]
Si-air battery	As-doped Si (100)	EMI·$(HF)_{2.3}$F + H_2O	300	1.45	~ 0.7	~200	[66]
Si-air battery	As-doped Si (100)	EMI·$(HF)_{2.3}$F + HEMA	100	1.45	0.6	850	[67]
Si-air battery	n-type nanostructured Si	KOH	100	1.3	1.2	days	[68]
Si-air battery	B-doped nanoporous Si	KOH	10	1.05	0.9	~13	[69]
Si-air battery	As-doped Si (111)	EMIm$(HF)_{2.3}$F	50	1.5	1.2–1.4	20	[64]
Si-air battery	As-doped Si (100)	KOH	50	1.4	1.2	1100	[71]
Si-air battery	As-doped Si (100)	KOH	10	1.4	1.35	24	[70]
Si-air battery	As-doped Si (100)	EMIm$(HF)_{2.3}$F	100	1.6	0.9	200	[65]
Ge-air battery	p-type nanoporous Ge	KOH	500	0.8	0.42	200	[72]
Ge-air battery	p^{+++} Ge	KOH	50	0.8	0.6	650	[74]
Ge-air battery	Ge (100)	KOH	1	0.95	0.92	24	[43]

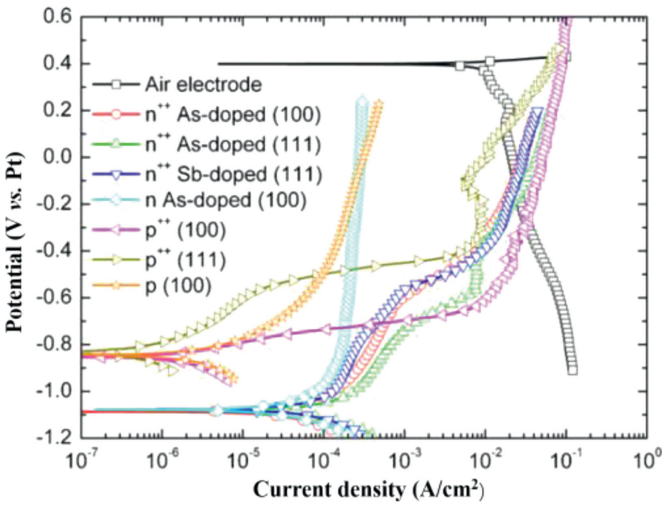

Fig. 3. Potentiodynamic polarization curves of As-, Sb-, and B-doped <100> and <111> oriented Si wafers and air cathode in EMIm(HF)2.3F solution. Copied with permission [63]. Copyright 2010, Elsevier.

cell were investigated by the galvanostatic polarization. The Si-air battery with an open circuit potential (OCP) of ~1.5 V discharged initially at 100 μA/cm^2 for 10 h and 50-300 μA/cm^2 for the next 120 h. Additional discharge process of 230 h was conducted at 100 μA/cm^2 exhibiting potential values of 1.25–0.9 V and a total capacity of 21 mAh. The discharge product was assumed to be SiO_2 which would deactivate the air cathode and terminate the discharging.

To further investigate the influences of the doping types and crystal orientations to battery performances, various silicon wafers named as n 100 (As), n^{++} 100 (As), n^{++} 111 (As), n^{++} 111 (Sb), p 100, p^{++} 100 and p^{++} 111 were tested by potentiodynamic experiments [63]. Potentials differences of 1.25–1.5 V were found between the air electrodes and Si anodes as shown in Fig. 3. The n^{++} (heavily doped n-type) silicon electrodes behaved similarly; however, the medium doped n-type anode exhibited the passivity. For p-type Si, the OCP values were 0.25–0.3 V more positive than the n-type anodes. In agreement with the previous work, n^{++} Si showed a larger potential distinction in the low current density region while the potential window was wider for p^{++} Si when the current density was > 1 mA/cm^2. What made the choice more complex was that p^{++} Si displayed lower corrosion rates hence longer life than the n^{++} type. The n^{++} 100 (As) Si was finally chosen to continue the research as the potential was crucial to optimize the battery characteristics. During the battery discharging, due to polarization losses the cell voltage dropped from 1.1 V to 0.8 V with increasing current density. The capacity of 53.4 mAh/cm^2 was obtained at the current density of 300 μA/cm^2 while the capacity value was only 6 mAh/cm^2 at 10 μA/cm^2. That phenomenon may result from different characteristics of the discharge products SiO_2 at various current densities. At lower current densities finer solid deposits would be produced on the porous carbon air electrode that blocked paths for oxygen diffusion and reduction. In contrast, oxygen diffusion would still be available when much coarser particles were deposited at higher current densities.

The effects of doping and orientation of Si anodes on the properties of the air batteries with EMIm$(HF)_{2.3}$F electrolyte were further investigated by Durmus's group [64]. The discharge abilities of anodes prepared from <100> and <111> oriented silicon wafers doped by As, Sb or B were evaluated under discharge current densities from 0.05 mA/cm^2 to 0.5 mA/cm^2. Si anodes with the As dopant exhibited the highest OCP of 1.5–1.6 V and discharge potentials regardless of the crystal orientation. Si anodes with B dopants independent of the orientations showed the lowest OCP of ~1.2 V. The Sb-doped Si anodes provided similar potentials under OCP and at low current densities with those of the As-doped; however, the behaviors approached the B-doped Si anodes at high current densities. With respect to the discharge potentials, the ranking of the Si anodes was shown below as:

$As_{100} > As_{111} \approx Sb_{100} > Sb_{111} \gg B_{100} > B_{111}$ at 0.05 mA/cm^2 and $As_{100} > As_{111} \gg Sb_{100} > B_{100} > B_{111} > Sb_{111}$ at 0.5 mA/cm^2.

The surface microstructures of the discharged anodes were also characterized, revealing the pronounced differences between the <100> and <111> oriented n-type Si anodes. Detailedly, the surfaces were rather homogenous for <100> oriented As- and Sb-doped Si, whereas the Si (111) electrodes produced visible polygons structures. For B-doped Si (100), the surface was smooth with only a few small pores after discharging with 0.1 mA/cm^2; in contrast, the <111> orientation or higher current densities would result in less smooth surfaces. The corrosion studies by mass loss measurements disclosed that the corrosion mass losses including chemical corrosion, electrochemical corrosion and other side reactions rise with the current density for both n- and p-type anodes. For n-type Si anodes, the mass losses of Si (111) were much lower (20% ~ 30%) than those of Si (100). Moreover, B-doped Si electrodes displayed lower losses compared with n-type Si anodes with <100> orientation. Considering anodic mass conversion efficiencies, the ranking was given as $B_{100} \approx B_{111} \approx As_{111} > Sb_{111} \gg Sb_{100} \approx As_{100}$.

Furthermore, the As-doped Si anodes exhibits the highest discharge energies contrast to the B-doped Si anodes and the highest specific energy of 1660 Wh/kg was realized for As-doped Si (111) anodes. Therefore, the corresponding ranking for specific energies was $As_{111} \gg As_{100} > Sb_{111} > B_{100} > B_{111} \approx Sb_{100}$.

Besides the operation of continuous discharge, pulsed discharge conditions were also conducted to investigate the behaviors of air

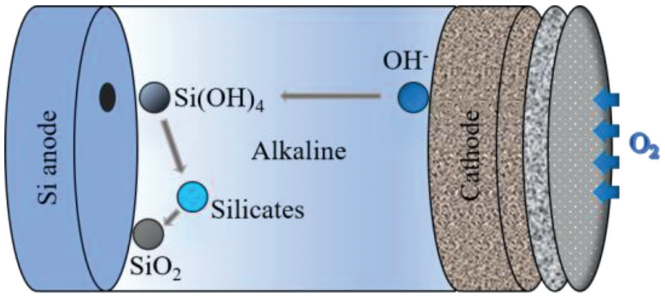

Fig. 4. The representation of the discharging processes of a typical Si-air battery with the alkaline electrolyte. .

batteries with <100> As-doped Si and <100> B-doped Si anodes [65]. Generally, the As-doped Si anodes had the advantages of open circuit voltage (OCV) and discharge voltages over B-doped anodes probably resulting from the variations on the Fermi levels. By the corrosion analysis, the Si anode doped by As corroded more readily than the B-doped Si during the OCV periods, and both kinds of anodes had higher corrosion rates along with the discharging at longer pulses, especially under a higher current density. At low to medium current pulse fractions, B-doped Si wafers offered higher specific energies (~ 1000 Wh/kg at $p = 0.25$). Correspondingly, Si anodes with As dopant behaved slightly better at medium to high current pulse. Overall, B-doped Si electrodes may be a better choice if cells would be operated dynamically.

In other respects, the influences of the water and polymer in ionic liquid (IL) electrolytes were investigated [66,67]. The water addition caused the shift of SiO_2 generation zone and the 15 vol% water led to the capacity increase of 40%. The capacity of the Si-air cell would apparently drop when the water content surpassed 20 vol%. The mixture of 10 vol% water-IL electrolyte exhibited a maximum in the ionic conductivity. The gel polymer electrolyte (GPE) containing 70 mol% IL and 2-hydroxyethyl methacrylate polymer showed a discharge voltage of 0.6 V over 850 h that would be beneficial for powering low power devices.

2.1.3. Aqueous batteries

Similar to non-aqueous batteries, the aqueous batteries consist of three main parts including the Si anode, alkaline solution electrolyte and carbon-based air cathode, as illustrated in Fig. 4. During the cell discharging, Si is oxidized to silicic acid ($Si(OH)_4$) *via* a four-electron process and then the reaction products would be probably ionized to $SiO_2(OH)_2^{2-}$ depending on the pH level.

In weak alkaline or neutral solutions, $Si(OH)_4$ would transfer into SiO_2. Concomitantly, the ORR occurs at the cathode generating hydroxide ions [41]. The whole electrochemical reactions are described as below Eqs. 5-8:

$$\text{Anode: } Si + 4OH^- \rightleftharpoons Si(OH)_4 + 4e^-,\ E^0 = -1.69\ V \quad (5)$$

$$\text{Formation of silicate: } Si(OH)_4 + 2OH^- \rightleftharpoons SiO_2(OH)_2^{2-} + 2H_2O \quad (6)$$

$$\text{Cathode: } O_2 + 2H_2O + 4e^- \rightleftharpoons 4OH^-,\ E^0 = 0.4\ V \quad (7)$$

$$\text{Corrosion: } Si + 2OH^- + 2H_2O \rightleftharpoons SiO_2(OH)_2^{2-} + 2H_2 \quad (8)$$

Theoretically, the alkaline Si-air cell has the voltage of 2.09 V since the half-cell potentials of cathode and anode are 0.4 V and −1.69 V *vs.* SHE, respectively. In practice, Duan's group reported the first alkaline Si-air battery which provided a working voltage of ~ 1.2 V [68]. Compared with planar Si wafers used before, the silicon surface was first modified by the metal-assisted electroless chemical etching method and silicon nanowire bundles with 1.5 μm thickness were fabricated on its surface. That kind of Si anode can be continuously discharged until the Si source was exhausted. In contrast, the cell using an unmodified wafer exhibited a discharging time of less than 10 min resulting from the quick surface passivation. The specific capacities with different current densities and electrolyte concentrations were analyzed and it can be concluded that lowering the electrolyte concentration would reduce the self-corrosion. The highest specific capacity of 1206 mAh/g can be reached with a diluted electrolyte concentration of 0.6 mol/L and current density of 0.1 mA/cm^2. In another work, Si nanowire (NW) was fabricated by the metal-assisted chemical etch process by Lee's group [69]. It was found that Si NWs would transform into Si nanopyramids (Si NPs) upon immersion in the alkaline solution or during the discharge of Si-air battery. The enhanced performance of the Si NW anode resulted from the formation of Si NPs with (111) facets that were intrinsically resistant to passivation.

Another work on modified Si anode was reported by Lee's group as visualized in Fig. 5 [70]. Nanoporous silicon (nPSi) electrodes were fabricated *via* electrochemical etching and the thickness and pore size of the porous layer can be controlled by modulating the etching time and ethanolic HF concentration. The galvanostatic discharge profiles showed that thicker porous layer and smaller pore diameter would lead to improved discharge capacity. It was demonstrated that more interaction between the Si surface and electrolyte was allowed due to the enlarged surface area.

To further investigate the corrosion rates and corrosion mechanisms in KOH solutions, highly As-doped Si wafers were used as anodes in Si-air cells [71]. At OCP, the corrosion mechanism was mainly chemical rather than electrochemical in nature and free H_2O molecules played a significant role in the chemical path. When in contact with KOH, Si corroded faster initially within the first hour; only after 8 h the steady-state conditions were maintained. That phenomenon resulted from the surface morphology evolution. As the activation energy for Si was 0.57 eV in 5 mol/L KOH, the corrosion was considered to be surface-reaction limited which was further assigned to be electron transfer. From the application aspect, low concentrated KOH electrolyte was beneficial for longer lifetime at OCP while higher concentrations were favorable under continuous discharge. A precondition of the continuous discharge process is to maintain the electrolyte in cells at an appropriate level, which was realized *via* a refill-type cell by Durmus's group [72]. The As-doped Si anode worked for more than 1100 h until it was exhausted thoroughly.

2.2. Ge-air batteries

2.2.1. Overview

Ge-air batteries were first reported by Lee's group in 2013 that exhibiting the OCP of ~0.8 V and discharging time beyond 200 h [73]. Encouraged by that work, Ge wafers with different doping types and crystal orientations were investigated as anodes in air batteries as summarized in Table 1. A typical Ge-air cell consists of Ge anode, KOH electrolyte and air diffusion electrode as visualized in Fig. 6. During the discharge process, Ge oxidation reaction and ORR happens in the anode and cathode respectively, accompanied by the anode surface passivation due to the dehydration of germanium hydroxide Eqs. 9–11:

$$\text{Anode}: Ge + 4OH^- \rightarrow Ge(OH)_4 + 4e^- \quad (9)$$

$$\text{Cathode}: O_2 + 2H_2O + 4e^- \rightarrow 4OH^-,\qquad E^0 = 0.4\ V \quad (10)$$

$$\text{Surface passivation}: Ge(OH)_4 \rightarrow GeO_2 + 2H_2O \quad (11)$$

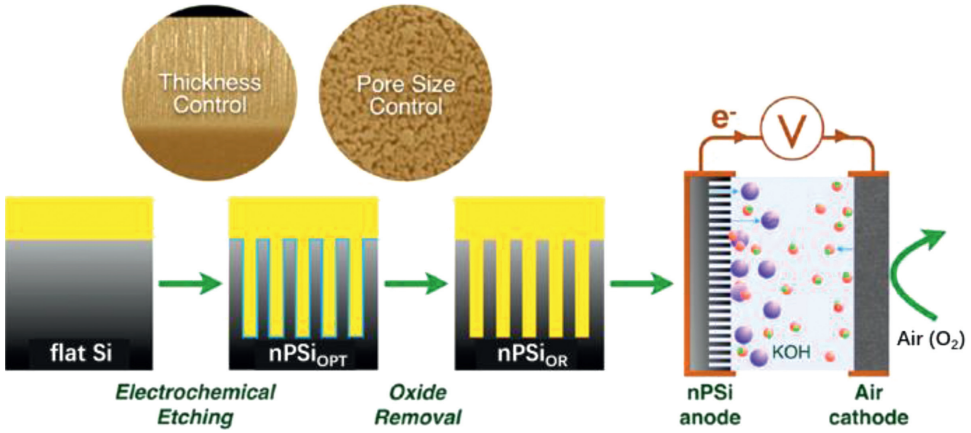

Fig. 5. The fabrication of nanoporous Si electrodes *via* electrochemical etching as anodes in Si-air batteries. Copied with permission [70]. Copyright 2015, American Chemical Society.

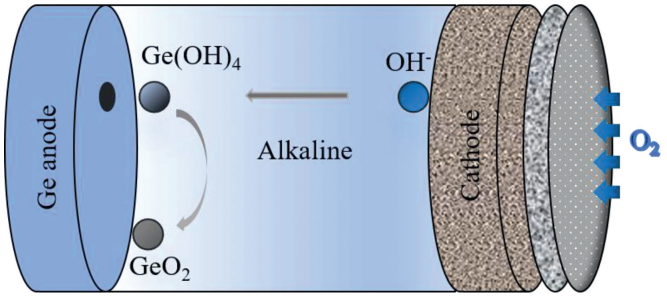

Fig. 6. The representation of the discharging processes of a typical Ge-air battery with the alkaline electrolyte.

The standard electromotive force of the Ge-air battery is ~1.0 V [73]. Besides experimental attempts, theoretical calculations on Ge-air batteries were also carried out by Yu's Group that would assist to comprehend the electrochemical properties fundamentally [74]. The researches on Ge-air batteries will be reviewed from experimental and theoretical points of view individually.

2.2.2. Experimental researches

Nanoporous germanium (PGe) produced from heavily doped p-type Ge (100) wafer was first used as an anode in the Ge-air battery [73]. The configurations of PGe were tuned by etching parameters such as the HF concentration, etching time and current density. Meanwhile the ratios of Ge and GeO_x were also modulated that would affect the discharge behavior. The OCP of combined electrochemical and electroless etched porous Ge (EE-ELE-PGe) was 0.8 V that was higher than that of pristine Ge (0.73 V). The EE-ELE-PGe also showed obvious improvements on the discharge time and working potential.

Besides the PGe, planar Ge wafers with different doping types and levels were investigated as anodes in the semiconductor-air cell [75]. The potentiodynamic curves showed that the n-type and p-type Ge anodes behaved similarly throughout the whole range of current densities, indicating their comparable discharge kinetics. The n-type Ge worked at higher voltages as the electrolyte concentration increased from 1 mol/L to 6 mol/L; in contrast, p-type Ge-air cells exhibited the highest voltage with the 3.0 mol/L KOH electrolyte. Compared with the flat discharge profile in p-type Ge-air batteries, the observed fluctuations of n-type Ge were suggested to arise from the interaction between the $Ge(OH)_4$ dissolution and surface passivation. From the Nyquist plots it can be concluded that p-type Ge had a smaller electrical resistance than n-type Ge after discharging for 8 h probably due to the lower rate of passivation on the surface. Furthermore, it was found that p-type Ge with heavier doping had better discharge kinetics. The understanding on the molecular level is still needed with the help of density functional theory (DFT) calculations. Lee's group also reported that discharge behaviors of the p-type Ge anodes were relevant to the crystal orientation [43]. The most negative onset potential was observed on Ge (111), followed by Ge (100) and Ge (110). The Ge-air cell with the (100) orientation operated at higher potentials (*e.g.*, 0.92 V at 1 μA/cm^2 and 0.4 V at 500 μA/cm^2), followed by Ge (111) and Ge (110). After 24 h of discharge, Ge (111) had the lowest resistance followed by Ge (100) and Ge (110), which was probably due to the different packing density of Ge atoms. The Ge (100) showed the highest maximum power density of 757.7 μW/cm^2 and the corresponding values of Ge (111) and Ge (100) were 519.9 μW/cm^2 and 496.9 μW/cm^2. The distinct performances may result from the surface oxidation and electrons flow affected by the crystal structure.

Although metal-air batteries offer high capacities, the anode utilization efficiencies in those cells (*i.e.*, Zn-air battery) are limited to only 60%. The immediate passivation of the metal anodes (*e.g.*, Mg, Al) during the discharge process makes the rest of the anode unusable. Actually, the capacity of Ge-air batteries is much higher that of commercial Zn-air cells (650 mAh/g_{Zn}, Energizer) and Al-air cells (320 mAh/g_{Al}, Altek Fuel Group Inc.), respectively [75]. In addition, the volumetric capacity of Ge-air batteries (7902 mAh/cm^3) is higher than most of the metal-air batteries as shown in Fig. 1 above.

2.2.3. Theoretical researches

To further understand the physics and chemistry of Ge-air batteries, it is crucial to investigate the surface passivation theoretically. Aiming at that, Yu's group constructed atomic model of Ge/GeO_2 interfaces with various crystal orientations and doping, and analyzed their properties by conducting DFT calculations [74]. According to the calculated binding energies of GeO_2 on the Ge (100) and Ge (111) surface, the surface passivation would be restrained on Ge (100) and that may be further hindered by the doping of anodes. Moreover, the I-V curves showed that the Ge (100)/GeO_2 interface exhibited a higher current than the Ge (111)/GeO_2 interface as visualized in Fig. 7.

3. Semiconductor cathodes in air batteries

3.1. Overview

Cathode is the other crucial unit in an air battery. The oxygen utilization of the cathode is the main factor affecting the discharge

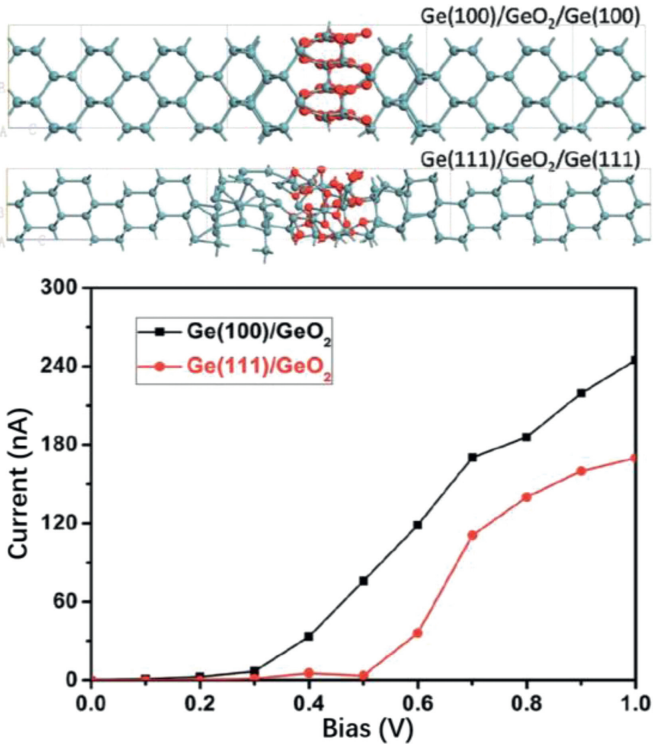

Fig. 7. The I-V curves of Ge (100)/GeO_2 and Ge (111)/GeO_2 interfaces. Copied with permission [74]. Copyright 2019, Royal Society of Chemistry.

efficiency, life span and actual specific energy of an air battery. The ORR of the cathode is a complex 4-electron or 2-electron reaction process with low reversibility, high overpotential and low current density (10^{-10} A/cm^2), which largely hinders the process of battery reaction and limits the efficiency of an air battery [17,58,76–78]. In most aqueous metal-air batteries using alkaline electrolytes and metals such as Zn, Mg, Fe and Al, ORR reaction happens through a $4e^-$ pathway producing OH^-. In comparison, $2e^-$ ORR reaction is the dominating way in certain nonaqueous metal-air batteries, such as Li-O_2 batteries. Recently, a Zn-O_2/ZnO_2 cell that proceeds through a $2e^-$ ORR process in nonalkaline aqueous electrolytes ($Zn(OTf)_2$) has been reported. That nonalkaline Zn-air battery not only tolerates stable operations in ambient air but also shows excellent reversibility [79]. The OER, as the reverse reaction of ORR, also plays a crucial role in a rechargeable air battery. Large amount of energy will lose during the OER because this reaction proceeds far from the equilibrium potential (1.23 V *vs.* NHE). Moreover, the evolution of O_2 easily causes the peeling of catalysts from the electrodes that would damage the electrochemical performance and the cycling stability of rechargeable air batteries. Therefore, the optimizing of cathodes for efficient ORR/OER is demanded to develop rechargeable air batteries.

Due to the slow kinetics of the ORR, the application of air battery-based energy devices in practice is greatly restricted. Pt-based catalysts can effectively accelerate the ORR rate and realize four-electron transfer; however, the large-scale commercialization of Pt-based catalysts is severely hindered by high-cost and lack of resource reserves. Therefore, it is of great significance to develop inexpensive catalysts with the ORR performance comparable to commercial Pt-based catalysts. Semiconductors, such as TiO_2, graphitic carbon nitride (g-C_3N_4), Fe_2O_3 and perovskites, have stable chemical and physical properties. They have been widely applied as cathodes in air batteries in recent years due to their nice abilities of harvesting solar, energy conversion, stability and low-cost [59,60,80–84]. Herein, we summarized semiconductors cathodes materials without and with photo-assistance in air batteries in recent three years.

3.2. Semiconductor cathodes without photo-assistance

Great progress has been made in the research and development of semiconductors as bifunctional catalysts. However, the low conductivity and agglomeration of metal oxide nanoparticles limit their ORR/OER activity. It is found that the problems of small specific surface area, poor conductivity and insufficient active sites of semiconductors can be handled by constructing nanostructures, combining with carbon materials or doping heterogeneous atoms [85–88]. For instance, Co_3O_4-doped Co/CoFe nanoparticles integrated with graphitic shells exhibited both high catalytic activity and stability due to the core-shell structure. The carbon shell effectively impeded the aggregation and further oxidation of Co/CoFe nanoparticles [89].

TiO_2 is a kind of transition metal oxide semiconductor that is usually adopted as the cathode materials for air battery due to its unique physicochemical properties, low-cost, environmental friendliness and simple preparation process [90–93]. There are three crystal types of TiO_2: Anatase, brookite and rutile. Among them, there are many studies on anatase, while brookite and rutile are relatively few. In 2018, Wang *et al.* synthesized atomic-thick TiO_2(B) nanosheets decorated with ultrafine Co_3O_4 nanocrystals and utilized them as cathode catalysts in Li-O_2 batteries. The Li-O_2 batteries showed a high specific capacity of 11,000 mAh/g and good cycling stability with low polarization [94]. In 2019, Zheng *et al.* fabricated oxygen vacancy-rich TiO_2 nanoparticles *in situ* on $Ti_3C_2T_x$ nanosheets. It was found that oxygen vacancy can improve the migration rate of electrons and Li^+ would act as the active sites for catalyzing the ORR and OER. That Li-O_2 battery exhibited an ultralow overpotential of 0.21 V, a high specific capacity of 11,487 mAh/g at the current density of 100 mA/g, and an excellent round-trip efficiency (93%) [93]. g-C_3N_4, due to its advantages of high nitrogen content (57 at%), sheet-like framework structure and large surface area, has focused much attention for ORR/OER in air batteries. Although the semiconductive property of g-C_3N_4 limits it to be an excellent electrocatalysis, it can be addressed by coupling with conductive substrates [94]. Besides, the pyridine-like N ligands can provide rich active link for metallic species, thus exerting synergistic effect between g-C_3N_4 matrix and metallic species for ORR/OER [95]. In 2019, Han *et al.* constructed the hybrid material of $NiCo_2S_4$ nanocrystal/g-C_3N_4 nanosheet/CNT for ORR/OER in Zn-air battery. Experimental studies revealed the electronic interactions between the abundant pyridinic-N species in underlying g-C_3N_4 and bimetallic Ni/Co active sites and identified the synergistic effect with coupled conductive CNTs to ameliorate reversible oxygen electrocatalysis [95].

Fe_2O_3 has been employed as the cathode material in air batteries because it is abundant and cost-effective. Fe_2O_3 has the similar shortages with the other semiconductors, *e.g.*, low intrinsic electronic conductivity. Usually, coupling with conductive materials like carbon materials has been demonstrated as an efficient method to improve the electronic conductivity [96,97]. For example, Jung *et al.* adopted carbon nanotube-bridged hollow Fe_2O_3 nanoparticles as the cathode of lithium-oxygen battery. Herein, hollow Fe_2O_3 NPs anchored by multiple CNTs provided promoted catalytic sites and fast charge-transport highway for facile formation and decomposition of Li_2O_2. The cell showed reversible cycling properties for 250 cycles with a fixed capacity of 1000 mAh/g at the current density of 500 mA/g. Besides, a module composed of two pouch-type cells could power a light-emitting diode lamp operated at 5.0 V stably [97].

The metal oxide of the perovskite crystal structure (ABO_3) is a commonly used bifunctional catalyst material, where A is gener-

Table 2
Summary of photocathode in Li-air/O_2 battery/Zn-air battery in recent three years.

Type of battery	Photocathode	Electrolyte	Current density	Charge potential (V) under irradiation	Cycle number	Total time (h)	Year/Ref.
Li-O_2 battery	ZnS-MWCNTs	TEGDME/ LiTFSI	100 mA/g	2.2	150	300	2018/[101]
Li-O_2 battery	WO_3 nanowires array	TEGDME/ $LiClO_4$	60 μA/cm^2	3.55	100	200	2019/[102]
Li-O_2 battery	C_3N_4/CP	TEGDME/ $LiClO_4$	100 μA/cm^2	3.38	10	20	2019/[103]
Li-O_2 battery	TiO_2 nanotube arrays and gold nanoparticles	TEGDME/ $LiCF_3SO_3$	50 μA/cm^2	2.67	200	6+	2020/[104]
Li-O_2 battery	TiO_2-Fe_2O_3	DMSO	10 μA/cm^2	3.2	50	100+	2020/[105]
Li-O_2 battery	WO_3@g-C_3N_4 NWA	TEGDME/ $LiClO_4$	100 μA/cm^2	3.69	100	200	2020/[106]
Li-O_2 battery	Ru NPs	LAGP	400 mA/g	3.5	50	2.5	2020/[107]
Li-O_2 battery	Biologically synthesized TiO_2 nanoparticles	TEGDME/ $LiClO_4$	100 mA/g	4.2	30	5	2021/[108]
Li-O_2 battery	Co-TABQ	LiTFSI/tetraglyme	100 μA/cm^2	3.32	50		2021/[109]
Zn-air battery	$Ni_{12}P_5$@NCNT	KOH/$Zn(Ac)_2$	10,000 μA/cm^2	1.9	500		2018/[110]
Zn-air battery	pTTh	KOH	20 mA/g	–	–	3	2019/[111]
Zn-air battery	pTTh	KOH	100 μA/cm^2	2	96	64	2019/[112]
Zn-air battery	CBPCNT	KOH	1000 μA/cm^2	1.88	–		2019/[113]
Zn-air battery	$BiVO_4$ or α-Fe_2O_3	KOH+$Zn(Ac)_2$	500 μA/cm^2	1.2 or 1.43	9 or 75	6 or 50	2019/[114]
Zn-air battery	PDTB/TiO_2	KOH	5000 μA/cm^2	0.59	–	22	2020/[115]

ally an alkaline earth metal or rare earth metal and B is a transition metal. Since its A site and B site can be partially replaced by other alkaline earth, rare earth metals or transition metals, the types of perovskite oxides are more abundant. Generally, the cubic crystal structure of perovskite oxides varies with its composition, thus showing different electrochemical activity. The ORR/OER activity of the perovskite-type catalysts mainly depends on the intrinsic characteristics of the transition metal ions. The introduction of different transition metal ions will form a certain degree of oxygen vacancies, which will generate more redox coupling electron pairs and lead to certain lattice defects. Therefore, they show excellent O anion mobility and exchange kinetic parameters [98]. The electrocatalytic active sites of perovskite-type bifunctional catalysts are usually considered to be cations located at the B site. Related researches show that when the B site is Co or Mn ion, the catalyst exhibits higher ORR/OER activity [98,99]. In 2018, Kim *et al.* prepared a bifunctional catalyst compositing of perovskite $LaCo_{0.8}Fe_{0.2}O_3$ nanowires with reduced graphene oxide sheets for lithium-oxygen battery cathodes. This catalyst exhibited an excellent discharge capacity (*ca.* 7088.2 mAh/g) at the first cycle and achieved a high stability of O_2-cathode which over 56 cycles under capacity limit of 500 mAh/g with a rate of 200 mA/g [100].

3.3. Semiconductor cathodes with photo-assistance

Adopting photo-responsive semiconductor as cathode can store photo-energy in the discharge/charge process that would bring down the overpotential and improve the reaction kinetics of air batteries, achieving combination of solar to electric energy and electric to chemical energy [59,60]. Based on this thinking, various endeavors were paid for searching and constructing efficient photo-responsive semiconductor cathodes in Li-air/O_2 and Zn-air batteries [101-115]. Herein, we mainly summarized the up-to-date photo-assisted semiconductor cathodes in Li-air/O_2 battery and Zn-air battery (Table 2), stated the relative configurations and photo-assisted working mechanisms and the merits of photo-energy during charging/discharging process, and provided the latest reported researches in this field.

3.3.1. Semiconductor cathodes in Li-air/O_2 batteries

The Li-air/O_2 battery has a high capacity and energy density. According to the calculation of negative electrode lithium, its theoretical energy density can reach ~3600 Wh/kg [100]. Besides, the theoretical value of the equilibrium potential of the organic Li-air/O_2 battery is 2.96 V, and its discharge platform value can reach *ca.* 2.7 V in practice. The ORR and OER in the charging and discharging processes of Li-air/O_2 batteries occur at the three-phase interface of electrode, electrolyte and O_2. Ignoring side reactions, the reaction equation for rechargeable organic Li-air/O_2 batteries can be described in Eq. 12 [103]:

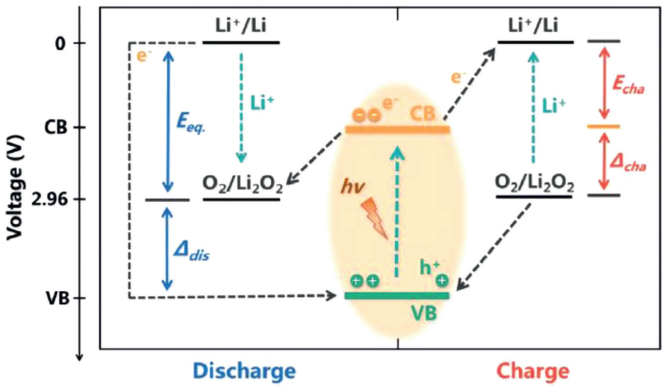

Fig. 8. Energy diagrams for the increased discharge voltage and decreased charge voltage of the Li-O_2 battery in light. Copied with permission [103]. Copyright 2019, Wiley-VCH.

$$2Li + O_2 \rightleftharpoons Li_2O_2,\ E^0 = 2.96\ V \quad (12)$$

However, due to the insoluble property and poor conductivity of Li_2O_2, the charging overpotential is high. Adopting photo-responsive semiconductor as cathode and introducing solar irradiation during ORR process can efficiently reduce the overpotential [59,60]. The working mechanism of a photo-assisted Li-air/O_2 battery without the redox reagent can be described as Eqs. 13–18 and illustrated in Fig. 8 (taken C_3N_4 as an example) [103]. This Li-O_2 battery consists of the Li metal anode, Li^+-conducting organic electrolyte and C_3N_4 cathode. The suitable energy levels (CB and VB position) of semiconductor ensure the sufficient utilization of photoelectrons and holes. Herein, the redox potential of O_2/Li_2O_2 is located between CB and VB of C_3N_4. During discharging under illumination, the photoelectrons reduce O_2 to O_2^-, and it then undergo a second electron reduction to O_2^{2-} and combine with Li^+ to produce Li_2O_2. Meanwhile, the holes in VB are reduced by the

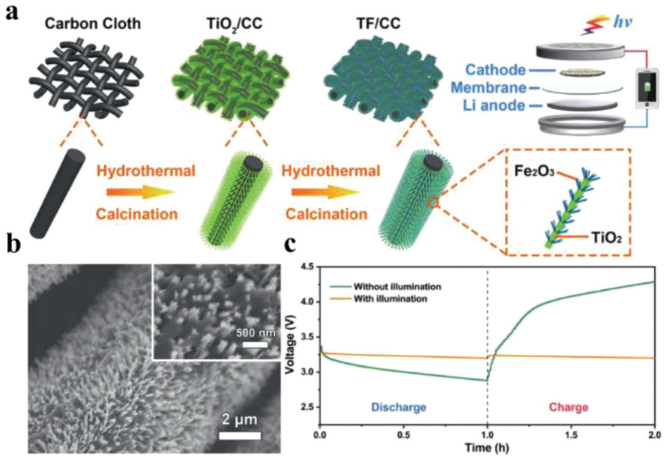

Fig. 9. (a) Schematic illustration of the synthesis procedure for the heterostructured TiO_2-Fe_2O_3 composite fabricated on carbon cloth (TF/CC) cathode and the structure of the photo-assisted Li-O_2 battery. (b) The SEM image of the TF/CC cathodes after being initially discharged with illumination. (c) The discharge and charge profiles of the Li-O_2 batteries with and without illumination at 0.01 mA/cm^2. Copied with permission [105]. Copyright 2020, Wiley-VCH.

electrons in the external circuit. The discharge voltage equals the potential difference between VB and Li^+/Li that is higher than the equilibrium of 2.96 V in Fig. 8. In the process of charging, the decomposition of Li_2O_2 is driven by the holes in VB and applied charge voltage, which propels the photoelectrons to move in the reverse direction via the external circuit to reduce Li^+ at anode. The charge voltage corresponds to the potential difference between CB and Li^+/Li that is lower than the equilibrium, as shown in Fig. 8. [103].

Discharge process:

$$\text{Lithium electrode}: Li - e^- \rightarrow Li^+ \quad (13)$$

$$\text{Air electrode}: O_2 + 2e^- \rightarrow O_2^{2-} \quad (14)$$

$$\text{Overall}: 2Li^+ + O_2^{2-} \rightarrow Li_2O_2 \quad (15)$$

Charge process:

$$\text{Air electrode}: \text{Semiconductor} + hv \rightarrow \text{Semiconductor} + e^- + h^+ \quad (16)$$

$$Li_2O_2 + h^+ \rightarrow 2Li^+ + O_2 \quad (17)$$

$$\text{Lithium electrode}: Li^+ + e^- \rightarrow Li \quad (18)$$

Yu *et al.* first developed a photo-assisted dye-sensitized TiO_2 photocathode for the Li-O_2 battery. By utilizing the photo-energy, photo-responsive semiconductor TiO_2 and triiodide/iodide redox shuttle, the charging overpotential was apparently reduced. This pioneering work offered a strategy to improve the energy efficiency and addressed the high charging overpotential issue for non-aqueous Li-O_2 battery [116]. In 2020, Li et al. established a hierarchical TiO_2-Fe_2O_3 heterojunction photocathode for the photo-assisted Li-O_2 battery as visualized in Fig. 9. TiO_2 was adopted as photocatalyst because of its excellent chemical stability and high photocorrosion resistance. Moreover, Fe_2O_3 with high chemical stability was chosen to regulate the electronic structure of TiO_2 for improved photoelectrochemical properties *via* heterostructural engineering. Due to the high light harvesting capability and electron-hole separation rate of TiO_2-Fe_2O_3 photocathode, the charging overpotential was largely reduced and the efficiency was obviously improved. The output and input energies of the battery provided an ultralow overpotential of 0.19 V between the charge and discharge plateaus with outstanding cyclic stability (retaining a round-trip efficiency of ~86% after 100 cycles) [105]. To tackle the problem that the long-time illumination will inevitably aggravate the degradation of the electrolyte, the super concentrated electrolyte composed of contact-ion-pairs was introduced presenting excellent stability against parasitic photocatalytic decomposition. By tuning the photocatalysis and Li_2O_2 electrochemical oxidization, the cycle life of rechargeable Li-O_2 batteries increased to 150 cycles [101].

3.3.2. Semiconductor cathodes in Zn-air batteries

Compared with electrochemical energy storage technologies, such as lithium-ion batteries, nickel-cadmium batteries, lead-acid batteries, and metal hydride batteries, Zn-air batteries have the advantages of high energy density (1086 Wh/kg in theory), high safety, low price, and environmental friendliness [113]. The Zn-air battery consists of the metal zinc negative electrode, electrolyte, and air electrode positive electrode. For rechargeable Zn-air battery, the metal zinc electrode is dissolved during the discharging process, and the discharge product is dissolved in the electrolyte to generate zinc oxide. When charging, the zinc oxide is reduced to metal zinc. With the help of the cathode catalyst, the O_2 participate in the ORR/OER and completing the conversion of electrical energy and chemical energy. The reaction equation for rechargeable Zn-air battery can be described in Eq. 19 [113]:

$$Zn + (1/2)O_2 \rightarrow ZnO \qquad E^0 = 1.65\ V \quad (19)$$

The standard electromotive force of the Zn-air battery is 1.65 V. However, due to the existence of polarization of ORR and the four/two electrons transfer steps at the cathode, the attainable output discharge voltage is 1.38 V at highest as well as the reaction kinetics is slow [111]. Introducing photons into Zn-air batteries can expedite the ORR process and improve the discharge voltage for high energy density [111,113]. Fig. 10 illustrates the working mechanism of the photo-assisted Zn-air battery [113]. This Zn-air battery consists of the Zn metal anode, alkaline electrolyte and a semiconductor ($BiVO_4$ or Fe_2O_3) air electrode. During discharging process, electrochemical oxidation of Zn to Zn^{2+} on the Zn electrode accompanied by the reduction of oxygen on the air electrode gives electricity output. During charging process under light illumination, the photogenerated electrons produced from CB of semiconductor rapidly transferred to the Zn electrode through the external circuit, resulting in the reduction of $Zn(OH)_4^{2-}$ to Zn. The photogenerated holes simultaneously migrate to the photoelectrode surface to oxidize OH^- to oxygen. The discharging and charging reactions can be illustrated by Eqs. 20–26 [113].

Discharge process:

$$\text{Zinc electrode}: Zn + 4OH^- \rightarrow Zn(OH)_4^{2-} + 2e^-, \quad E^0 = -1.25\ V \quad (20)$$

$$Zn(OH)_4^{2-} \rightarrow ZnO + H_2O + 2OH^- \quad (21)$$

$$\text{Air electrode}: O_2 + 2H_2O + 4e^- \rightarrow 4OH^-, \quad E^0 = 0.4\ V \quad (22)$$

$$\text{Overall}: 2Zn + O_2 \rightarrow 2ZnO, \quad E^0 = 1.65\ V \quad (23)$$

Charge process:

$$\text{Zinc electrode}: Zn(OH)_4^{2-} + 2e^- \rightarrow Zn + 4OH^- \quad (24)$$

$$\text{Air electrode}: \text{Photoelectrode} + hv \rightarrow e^- + h^+ \quad (25)$$

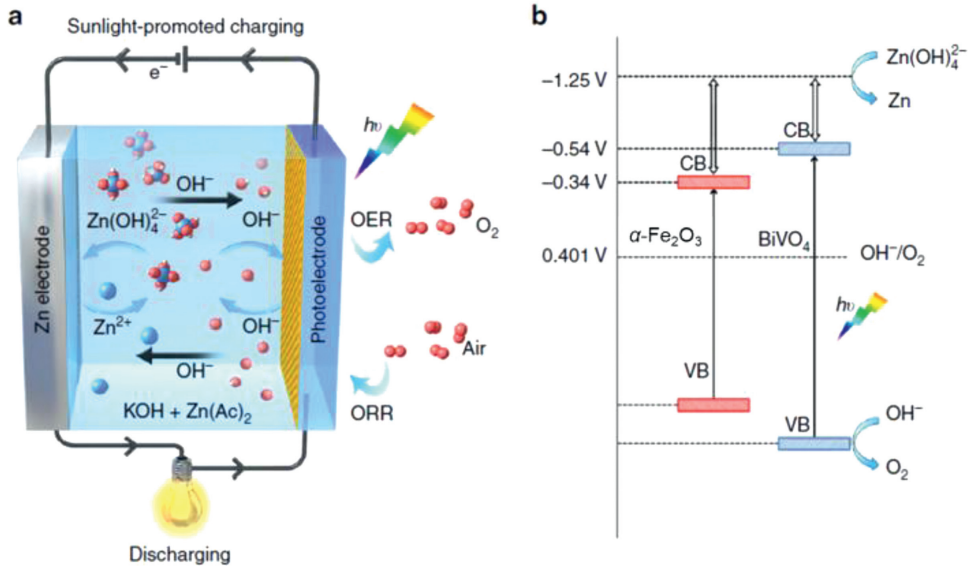

Fig. 10. Schematic sunlight-promoted charge and discharge processes of the sunlight-promoted Zn-air battery. (a) The scheme of the basic structure and working principle of the sunlight-promoted rechargeable Zn-air battery. (b) The proposed mechanism of the sunlight-promoted charging process under solar light illumination. Copied with permission [113]. Copyright 2019, Nature Publishing Group.

$$4OH^- + 4h^+ \rightarrow 2H_2O + O_2 \quad (26)$$

In 2019, Liu *et al.* adopted semiconductor $BiVO_4$ and α-Fe_2O_3 as cathode in Zn-air batteries [113]. With photo-assistance, the batteries achieved record-low charge voltages of ~1.20 and ~1.43 V, respectively, which were lowered by 0.5–0.8 V compared with conventional Zn-air batteries. The band structure and photoelectrochemical stability of the semiconductor cathode played an important role in the photo-assisted Zn-air battery with a high energy efficiency. In 2020, Du *et al.* used two semiconducting poly(1,4-di(2-thienyl))benzene (PDTB) and TiO_2 cathodes to clamp a Zn anode in the Zn-air battery [114]. During the discharging, the photoelectrons in the CB of PDTB were donated to O_2 for its reduction to $O_2^{\bullet-}$ that then converted to OH^-, and the holes left behind in the VB were transferred for the oxidation of Zn to ZnO. In the charge process on TiO_2, the holes were driven by an applied voltage for oxidation of OH^- to $^{\bullet}OH$, and then it decomposed to produce O_2. A record-high discharge voltage of 1.90 V and an unprecedented low charge voltage of 0.59 V were achieved in the photo-involved Zn-air battery.

4. Conclusions and outlook

This review aims to summarize the developments of Si-air batteries and Ge-air batteries briefly, and render a snapshot of recent advances in semiconductor cathodes of air batteries. Despite the intense researches on semiconductors, many efforts are still needed for further advancement of these novel energy technologies of air batteries. The challenges of the semiconductor anodes in the future application are discussed as below: (a) Pure Si wafers that are commonly used in Si-air batteries as anodes have the drawback of high corrosion rates. Consequently, the self-discharge is not restrained and only ~30% of Si-air battery's theoretical energy capacity has been reported in practice. (b) In both Si-air battery and Ge-air battery, anode surface passivation would happen when $Si(OH)_4$ or $Ge(OH)_4$ transfers into SiO_2 or GeO_2 during the discharge. The oxide layer may prevent the contact between the anode and electrolyte and cease the discharge process. (c) Compared with metal anodes, the conductivities of semiconductor anodes (especially Si) are limited that may restrain the discharge kinetics. (d) Si and Ge wafers are brittle and Ge wafer costs much. (e) Currently, Si-air and Ge-air batteries are almost primary batteries. Their application scenes would be extended if the cycling of semiconductor-air batteries can be realized conveniently.

Prospective research directions of semiconductors in air batteries could focus on the following:

For Si-air and Ge-air batteries, planar Si and Ge wafers are currently most common anode materials. To further enhance the performances, micro/nano-structure Si and Ge anodes should be fabricated that may hinder the surface passivation and enhance the discharge time. The formation of SiO_2 and GeO_2 passivation layer on the anode surface can be further modulated to ensure the sustained contact between the anode and electrolyte. The anode surface modifications by additives may be effective solutions to protect the anodes. To enhance the conductivity, semiconductor wafers with B, As and Sb dopants can be used as anodes; semiconductor anodes can be composited by a conductive layer; Si or Ge can be alloyed with some metals. Si-air batteries and Ge-air batteries have distinct advantages. Si-air batteries have a higher theoretical capacity (3822 mAh/g_{Si}) than Ge-air batteries (1477 mAh/g_{Ge}) and cost less. However, Ge-air batteries have a higher actual specific capacity (1302.5 mAh/g_{Ge}) than Si-air batteries (1206 mAh/g_{Si}). An extremely high anode utilization of ~88% can be derived in Ge-air batteries. Compared with Si-air batteries, Ge-air batteries have better discharge kinetics that result in a much higher actual power density. Si-Ge composite anodes may provide advantages which are inherent to each battery. Flexible Si-air and Ge-air batteries are also desirable. Besides traditional Pt/C catalysts, novel ORR catalysts should be synthesized and applied in the Si- and Ge-air batteries to improve the kinetics of air electrodes. Simulations of Si-air and Ge-air batteries like DFT calculations and finite-element analysis are also on urgent demands to provide deeper comprehension of discharge mechanisms and optimal designs of batteries.

For semiconductor cathodes, the stability of the catalyst materials should be improved. In traditional metal air batteries, to restrain the irreversible change of bi-functional catalysts during cycling, many efforts have been paid to enhance the durability of the non-noble metal based catalysts. The catalysts can be doped with heteroatoms (*e.g.*, Zn, Ni and S), as well as composited with other

metal (oxides) such as MnO_2, Co or carbon materials. The reported cycle life of photo-assisted air batteries is still limited. One possible reason is the decomposition of electrolytes induced by illumination. Additionally, the stabilities of photocatalysts during cycling conditions are still less investigated, especially the synergetic effects of electrolytes and photocatalysts under a long period of illumination. Therefore, exploring durable photoelectrode and electrolytes with excellent photostability and electrochemical stability is critically important to photo-assisted air batteries. It is worth noticing that solid-state electrolytes exhibit superior photostability and safety. From this perspective, developing photo-responsive all-solid-state batteries would be reasonable to achieve stabilized systems. Meanwhile, the cathode configuration should be optimized with transparent and porous materials to guarantee sufficient exposure of both light and oxygen. Moreover, test conditions such as illumination wavelength and power density should be standardized to compare the properties of different materials conveniently. Finally, theoretical investigations on ORR/OER with different semiconductor materials are inevitably necessary.

In summary, the exploration of semiconductors in air batteries is still in the early stage. With the help of semiconductors, it is believed that air batteries will be widely applied in MEMS and photo-electrochemical devices. The researches will be beneficial for developing other novel energy storage and conversion systems as well.

Declaration of competing interest

The authors declare that they have no known competing financial interests or personal relationships that could have appeared to influence the work reported in this paper.

Acknowledgments

This work is financially supported by the National Nature Science Foundation of China (Nos. 61904073 and 62004085), the Projects of Science and Technology Plans of Kunming (No. 2019-1-C-25318000002189), Applied Basic Research Programs of Yunnan Science and Technology Department (No. 2019FGF02), the Spring City Plan-Special Program for Young Talents (No. ZX20210014), the Talents Introduction Project of Kunming University (Nos. YJL18008 and YJL16003).

References

[1] M. Meinshausen, Z.R.J. Nicholls, J. Lewis, et al., Geosci. Model Dev. 13 (2020) 3571–3605.
[2] S. Maddukuri, D. Malka, M.S. Chae, et al., Electrochim. Acta 354 (2020) 136771.
[3] M. Armand, P. Axmann, D. Bresser, et al., J. Power Sources 479 (2020) 228708.
[4] A. Chitre, D. Freake, L. Lander, J. Edge, M.M. Titirici, Batteries Supercaps 3 (2020) 1125.
[5] D. Stampatori, P.P. Raimondi, M. Noussan, Energies 13 (2020) 2638.
[6] E. Fan, L. Li, Z. Wang, et al., Chem. Rev. 120 (2020) 7020–7063.
[7] H. Lv, H. Huang, C. Huang, et al., Appl. Catal. B 283 (2021) 119634.
[8] Y. Kim, W.M. Seong, A. Manthiram, Energy Storage Mater. 34 (2021) 250–259.
[9] Y. Tian, G. Zeng, A. Rutt, et al., Chem. Rev. 121 (2021) 1623–1669.
[10] F. Wu, J. Maier, Y. Yu, Chem. Soc. Rev. 49 (2020) 1569–1614.
[11] Y. Zhang, T.-.T. Zuo, J. Popovic, Mater. Today 33 (2020) 56–74.
[12] J. Zhang, G. Zhang, Z. Chen, et al., Energy Storage Mater. 26 (2020) 513–533.
[13] Q. Gou, S. Zhao, J. Wang, M. Li, J. Xue, Nano-Micro Lett. 12 (2020) 98.
[14] T. Wang, C. Li, X. Xie, et al., ACS Nano 14 (2020) 16321–16347.
[15] C. Yang, S. Xin, L. Mai, Y. You, Adv. Energy Mater. 11 (2021) 2000974.
[16] C. Zhang, H. Zhao, Y. Lei, Energy Environ. Mater. 3 (2020) 105–120.
[17] Q. Liu, Z. Pan, E. Wang, L. An, G. Sun, Energy Storage Mater. 27 (2020) 478–505.
[18] H.F. Wang, Q. Xu, Matter 1 (2019) 565–595.
[19] N. Chawla, Mater. Today Chem. 12 (2019) 324–331.
[20] X. Chen, I. Ali, L. Song, et al., Renew. Sustain. Energy Rev. 134 (2020) 110085.
[21] J. Yu, B.Q. Li, C.X. Zhao, Q. Zhang, Energy Environ. Sci. 13 (2020) 3253–3268.
[22] Y. Wang, Y.C. Lu, Energy Storage Mater. 28 (2020) 235–246.
[23] W.J. Kwak, D.Sharon Rosy, et al., Chem. Rev. 120 (2020) 6626–6683.
[24] T. Liu, J.P. Vivek, E.W. Zhao, et al., Chem. Rev. 120 (2020) 6558–6625.
[25] S. Zhao, L. Li, F. Li, S.-.L. Chou, Electrochem. Commun. 118 (2020) 106797.
[26] H. Yadegari, X. Sun, Trends Chem. 2 (2020) 241–253.
[27] X. Xu, K.S. Hui, D.A. Dinh, K.N. Hui, H. Wang, Mater. Horiz. 6 (2019) 1306–1335.
[28] F. Duffner, N. Kronemeyer, J. Tubke, et al., Nat. Energy 6 (2021) 123–134.
[29] D. Stock, S. Dongmo, J. Janek, D. Schröder, ACS Energy Lett. 4 (2019) 1287–1300.
[30] T. Zhou, N. Zhang, C. Wu, Y. Xie, Energy Environ. Sci. 13 (2020) 1132–1153.
[31] L. Lei, Y. Sun, X. Wang, Y. Jiang, J. Li, Front. Mater. 7 (2020) 96.
[32] J. Hao, X. Li, X. Zeng, et al., Energy Environ. Sci. 13 (2020) 3917–3949.
[33] Z. Zhao, X. Fan, J. Ding, et al., ACS Energy Lett. 4 (2019) 2259–2270.
[34] D.Dobhal P.Goel, R.C. Sharma, J. Energy Storage 28 (2020) 101287.
[35] Y. Hu, D. Sun, B. Luo, L. Wang, Energy Technol 7 (2019) 86–106.
[36] X. Zhang, R. Lv, W. Tang, et al., Adv. Funct. Mater. 30 (2020) 2004187.
[37] Y. Liu, Q. Sun, W. Li, et al., Green Energy Environ. 2 (2017) 246–277.
[38] T. Zhang, Z. Tao, J. Chen, Mater. Horiz. 1 (2014) 196–206.
[39] Y. Sun, X. Liu, Y. Jiang, et al., J. Mater. Chem. A 7 (2019) 18183–18208.
[40] Z. Guo, S. Zhao, T. Li, et al., Adv. Energy Mater. 10 (2020) 1903591.
[41] H. Weinrich, Y.E. Durmus, H. Tempel, H. Kungl, R.A. Eichel, Materials (Basel) 12 (2019) 2134.
[42] R. Bansal, P. Menon, R.C. Sharma, SN Appl. Sci. 2 (2020) 1141.
[43] J.D. Ocon, G.H.A. Abrenica, J. Lee, ChemElectroChem 3 (2016) 242–246.
[44] J. Li, C. Yue, Y. Yu, et al., J. Mater. Chem. A 1 (2013) 14344–14349.
[45] Y. Yu, C. Yue, S. Sun, et al., ACS Appl. Mater. Interfaces 6 (2014) 5884–5890.
[46] Y. Yu, C. Yue, X. Lin, et al., ACS Appl. Mater. Interfaces 8 (2016) 3992–3999.
[47] Y. Yu, Y. Wang, S. Zhang, et al., Nano Energy 61 (2019) 604–610.
[48] J. Mei, T. Liao, J. Liang, et al., Adv. Energy Mater. 10 (2020) 1901997.
[49] J.W. Jung, S.H. Cho, J.S. Nam, I.D. Kim, Energy Storage Mater. 24 (2020) 512–528.
[50] M. Balaish, J.W. Jung, I.D. Kim, Y. Ein-Eli, Adv. Funct. Mater. 30 (2020) 1808303.
[51] S. Yang, Y. Cheng, X. Xiao, H. Pang, Chem. Eng. J. 384 (2020) 123294.
[52] J. Liu, H. Liu, H. Chen, et al., Adv. Sci. 7 (2019) 1901614.
[53] F. Shi, X. Zhu, W. Yang, Chin. J. Catal. 41 (2020) 390–403.
[54] L. Peng, L. Shang, T. Zhang, G.I.N. Waterhourse, Adv. Energy Mater. 10 (2020) 2003018.
[55] M. Luo, W. Sun, B.B. Xu, H. Pan, Y. Jiang, Adv. Energy Mater. 11 (2021) 2002762.
[56] Y. Wang, Q. Cao, C. Guan, C. Cheng, Small 16 (2020) 2002902.
[57] A. Zahoor, Z.K. Ghouri, S. Hashmi, et al., ACS Sustainable Chem. Eng. 7 (2019) 14288–14320.
[58] Y. Guo, Y.N. Chen, H. Cui, Z. Zhou, Chin. J. Catal. 40 (2019) 1298–1310.
[59] Z. Fang, X. Hu, D. Yu, Chempluschem 85 (2020) 600–612.
[60] P. Tan, X. Xiao, Y. Dai, C. Cheng, M. Ni, Renew. Sustain. Energy Rev. 127 (2020) 109877.
[61] A. Gurung, Q. Qiao, Joule 2 (2018) 1217–1230.
[62] G. Cohn, D. Starosvetsky, R. Hagiwara, D.D. Macdonald, Y. Ein-Eli, Electrochem. Commun. 11 (2009) 1916–1918.
[63] G. Cohn, Y. Ein-Eli, J. Power Sources 195 (2010) 4963–4970.
[64] Y.E. Durmus, S. Jakobi, T. Beuse, Ö. Aslanbas, et al., J. Electrochem. Soc. 164 (2017) A2310–A2320.
[65] Y.E. Durmus, C. Roitzheim, H. Tempel, et al., J. Appl. Electrochem. 50 (2020) 93–109.
[66] G. Cohn, D.D. Macdonald, Y. Ein-Eli, ChemSusChem 4 (2011) 1124–1129.
[67] G. Cohn, A. Altberg, D.D. Macdonald, Y. Ein-Eli, Electrochim. Acta 58 (2011) 161–164.
[68] X. Zhong, H. Zhang, Y. Liu, et al., ChemSusChem 5 (2012) 177–180.
[69] S. Sarwar, M. Kim, G. Baek, I. Oh, H. Lee, Bull. Korean Chem. Soc. 37 (2016) 997–1003.
[70] D.W. Park, S. Kim, J.D. Ocon, et al., ACS Appl. Mater. Interfaces 7 (2015) 3126–3132.
[71] Y.E. Durmus, S.S.M. Guerrero, Ö. Aslanbas, et al., Electrochim. Acta 265 (2018) 292–302.
[72] Y.E. Durmus, Ö. Aslanbas, S. Kayser, et al., Electrochim. Acta 225 (2017) 215–224.
[73] J.D. Ocon, J.W. Kim, S. Uhm, B.S. Mun, J. Lee, Phys. Chem. Chem. Phys. 15 (2013) 6333–6338.
[74] Y. Yu, D. Chen, S. Gao, et al., RSC Adv. 9 (2019) 39582–39588.
[75] J.D. Ocon, J.W. Kim, G.H.A. Abrenica, J.K. Lee, J. Lee, Phys. Chem. Chem. Phys. 16 (2014) 22487–22494.
[76] Y. Dong, S. Li, S. Hong, L. Wang, B. Wang, Chin. Chem. Lett. 31 (2020) 635–642.
[77] J. Tian, D. Liu, J. Li, et al., Chin. Chem. Lett. 32 (2021) 2427–2432.
[78] Y. Ren, H. Wang, T. Zhang, et al., Chin. Chem. Lett. 32 (2021) 2243–2248.
[79] W. Sun, F. Wang, B. Zhang, et al., Science 371 (2021) 46–51.
[80] J. Hu, C. Zhai, M. Zhu, Chin. Chem. Lett. 32 (2021) 1348–1358.
[81] Y. Chen, S. Lan, M. Zhu, Chin. Chem. Lett. 32 (2021) 2052–2056.
[82] M. Zhang, J. He, Y. Chen, et al., Chin. Chem. Lett. 31 (2020) 2721–2724.
[83] S. Hu, Y. Yu, Y. Guan, et al., Chin. Chem. Lett. 31 (2020) 2839–2842.
[84] H. Zhang, J. He, C. Zhai, M. Zhu, Chin. Chem. Lett. 30 (2019) 2338–2342.
[85] M. Nehra, N. Dilbaghi, G. Marrazza, Nano Energy 76 (2020) 104991.
[86] X. Li, D. Liu, X. Mo, K. Li, J. Solid State Electrochem. 23 (2019) 2843–2852.
[87] J. Li, Z. Meng, D.J.L. Brett, et al., ACS Appl. Mater. Interfaces 12 (2020) 42696–42703.
[88] X. Shu, S. Chen, S. Chen, W. Pan, J. Zhang, Carbon N Y 157 (2020) 234–243.
[89] T. Li, Y. Lu, S. Zhao, Z. Gao, Y. Song, J. Mater. Chem. A 6 (2018) 3730–3737.

[90] S. Pakseresht, T. Cetinkaya, A.W.M. Al-Ogaili, M. Halebi, H. Akbulut, Ceram. Int. 47 (2021) 3994–4005.
[91] F. Li, Y. Wang, R.S. Bai, et al., J. Power Sources 483 (2021) 229180.
[92] G. Wang, S. Zhang, R. Qian, Z. Wen, ACS Appl. Mater. Interfaces 10 (2018) 41398–41406.
[93] R. Zheng, C. Shu, Z. Hou, et al., ACS Appl. Mater. Interfaces 11 (2019) 46696–46704.
[94] L. Zhang, J. Xiong, Y.H. Qin, C.W. Wang, Carbon N Y 150 (2019) 475–484.
[95] X. Han, W. Zhang, X. Ma, et al., Adv. Mater. 31 (2019) 1808281.
[96] Y. Tian, J.Qian L.Xu, et al., Carbon N Y 146 (2019) 763–771.
[97] J.W. Jung, J.S. Jang, T.G. Yun, K.R. Yoon, I.D. Kim, ACS Appl. Mater. Interfaces 10 (2018) 6531–6540.
[98] D. Chen, C. Chen, Z.M. Baiyee, Z. Shao, F. Ciucci, Chem. Rev. 115 (2015) 9869–9921.
[99] W.G. Hardin, J.T. Mefford, D.A. Slanac, et al., Chem. Mater. 26 (2014) 3368–3376.
[100] J.G. Kim, Y. Kim, Y. Noh, et al., ACS Appl. Mater. Interfaces 10 (2018) 5429–5439.
[101] Y. Qiao, Y. Liu, K. Jiang, et al., Small Methods 2 (2018) 1700284.
[102] Y. Feng, H. Xue, T. Wang, et al., ACS Sustain. Chem. Eng. 7 (2019) 5931–5939.
[103] Z. Zhu, X. Shi, G. Fan, F. Li, J. Chen, Angew. Chem. 131 (2019) 19197–19202.
[104] S. Tong, C. Luo, J. Li, et al., Angew. Chem. 132 (2020) 21095–21099.
[105] M. Li, X. Wang, F. Li, et al., Adv. Mater. 32 (2020) 1907098.
[106] H. Xue, T. Wang, Y. Feng, et al., Nanoscale 12 (2020) 18742–18749.
[107] H. Song, S. Wang, X. Song, et al., Energy Environ. Sci. 13 (2020) 1205–1211.
[108] S. Pakseresht, T. Cetinkaya, A.W.M. Al-Ogaili, M. Halebi, H. Akbulut, Ceram. Int. 47 (2021) 3994–4005.
[109] Q. Lv, Z. Zhu, S. Zhao, et al., J. Am. Chem. Soc. 143 (2021) 1941–1947.
[110] J. Lv, S.C. Abbas, Y. Huang, et al., Nano Energy 43 (2018) 130–137.
[111] K. Wang, Z. Mo, S. Tang, et al., J. Mater. Chem. A 7 (2019) 14129–14135.
[112] D. Zhu, Q. Zhao, G. Fan, et al., Angew. Chem. Int. Ed. 58 (2019) 12460–12464.
[113] Z. Fang, Y. Zhang, X. Hu, et al., Angew. Chem. Int. Ed. 58 (2019) 9248–9253.
[114] X. Liu, Y. Yuan, J. Liu, et al., Nat. Commun. 10 (2019) 4767.
[115] D. Du, S. Zhao, Z. Zhu, F. Li, J. Chen, Angew. Chem. Int. Ed. 59 (2020) 18140–18144.
[116] M. Yu, X. Ren, L. Ma, Y. Wu, Nat. Commun. 5 (2014) 5111.